Transactions on Energy Systems and Engineering Applications

Article

Techno-economic assessment of a low-frequency AC transmission interconnection for an offshore wind farm in Colombia

Cristian Bernal[1], Valentina Fragozo[1], Iván Ortega[1], Rafael Castillo-Sierra[1], Mauricio Restrepo[1] and Juan Diego Pulgarín Rivera[2]

[1] División de Ingenierías, Universidad del Norte, Barranquilla, Colombia.
[2] Facultad de Ingeniería, Universidad Distrital Francisco José de Caldas, Bogotá, Colombia.
* Correspondence: rcastilloj@uninorte.edu.co

Received: 19 January 2026; Accepted: 14 May 2026; Published: 17 June 2026

Abstract: Colombia's Caribbean coast has substantial offshore wind potential but lacks dedicated transmission infrastructure. Although high-voltage AC (HVAC) and high-voltage DC (HVDC) are established solutions, low-frequency AC (LFAC)—the transmission of power at frequencies below the standard 50 or 60 Hz—offers a cost-effective alternative for medium-distance applications. This study assesses an LFAC system to connect a 960 MW offshore wind farm to the national 60 Hz grid under Colombian regulatory and geographic conditions. The proposed LFAC link operates at 20 Hz and includes a 75 km submarine cable, a 34 km overhead line, and a back-to-back modular multilevel converter working as a frequency conversion station. The design meets national limits on voltage regulation and unbalance, and considers efficiency, shunt currents, and transfer capability. Performance was validated using `MATLAB/Simulink` simulations under variable load. The economic analysis compares capital expenditure (CAPEX) and loss-related costs with HVAC and HVDC. The system achieved over 93% efficiency and complied with all voltage standards. Compared to 60 Hz HVAC, the 20 Hz LFAC enabled roughly 200% more transfer capacity and reduced shunt currents by 66%, improving stability. LFAC's CAPEX was 9.4% higher than HVAC but 8.1% lower than HVDC. LFAC is technically and economically viable for offshore wind integration in Colombia, bridging HVAC's reactive limitations and HVDC's high costs, and is scalable for similar renewable projects worldwide.

https://doi.org/10.32397/tesea.vol7.n1.970

How to cite this article: Bernal, Cristian; Fragozo, Valentina; Ortega, Iván; Castillo-Sierra, Rafael; Restrepo, Mauricio; Pulgarín Rivera, Juan Diego. Techno-economic assessment of a low-frequency AC transmission interconnection for an offshore wind farm in Colombia. *Transactions on Energy Systems and Engineering Applications*, 7(1): 970, 2026. DOI:10.32397/tesea.vol7.n1.970

1. Introduction

1.1. General Context and Motivation

The global energy sector is undergoing a profound transformation aimed at reducing greenhouse gas emissions and fostering long-term sustainability. In line with this transition, Colombia has introduced policies such as Law 1715 of 2014 [1], which promotes the integration of non-conventional renewable energy sources into the national electricity matrix. Offshore wind energy stands out due to Colombia's vast technical potential along the Caribbean coast, estimated to exceed 100 GW [2], yet no offshore wind farms or dedicated transmission infrastructure have been deployed. Low-Frequency AC (LFAC) transmission has emerged internationally as an alternative to conventional HVAC and HVDC solutions for medium-distance offshore connections [3–5], but its applicability and benefits under Colombia's specific regulatory, environmental, and geographic conditions have not been widely studied. Moreover, similar challenges related to offshore wind integration and transmission system selection may arise in other coastal regions with emerging energy systems, suggesting that the Colombian case can also provide insights beyond a purely national context.

1.2. Brief Literature Review

Offshore wind farm integration has traditionally relied on HVAC and HVDC transmission technologies. HVAC connections are well-suited for short distances but suffer from significant reactive power consumption and capacitive charging currents in submarine cables beyond 50–80 km [6,7]. In contrast, HVDC links can transmit power efficiently over long distances, but their high converter station costs and operational complexity make them less attractive for medium-distance projects [3,4,8,9].

LFAC transmission has emerged as an intermediate solution, reducing cable charging currents by operating at frequencies well below the standard 50/60 Hz [10,11]. Studies have demonstrated that LFAC can extend the feasible range of AC submarine transmission while retaining simpler protection and operational schemes compared to HVDC [12,13]. Recent works have evaluated LFAC for offshore wind integration in Europe, North America, and Asia [12,13]; however, its performance and economic viability have not yet been examined under the specific regulatory, environmental, and geographic conditions of Colombia. Furthermore, most existing studies focus on developed regions with mature grid infrastructures, with limited attention to developing coastal regions where grid constraints, investment limitations, and medium-distance offshore wind resources may be present. In this context, assessing LFAC performance in Colombia may also provide insights relevant to other regions, such as Southeast Asia, West Africa, and other countries of Latin America. Evaluating LFAC performance and costs for a Colombian offshore wind project allows stakeholders to compare it directly with HVAC and HVDC alternatives, offering practical evidence to guide future large-scale integration strategies in the country. While the analysis is based on a Colombian case study, the proposed framework and findings may also offer insights applicable to other coastal regions with comparable offshore wind integration challenges. This study combines detailed electrical modeling, dynamic simulations, route analysis, and a comparative economic assessment to provide decision-makers with information relevant to technical planning and policy formulation.

1.3. Paper Contributions

This work provides a comprehensive techno-economic evaluation of a 20 Hz LFAC transmission system for integrating large-scale offshore wind energy into the Colombian power grid, considering real technical, regulatory, and geographical constraints. The main contributions are:

1. Development and simulation of a detailed electrical model of a 960 MW LFAC interconnection, including a submarine cable, overhead line, and back-to-back modular multilevel converter (MMC), validated against Colombian grid code requirements.
2. Comparative performance assessment of LFAC and HVAC alternatives under identical route and loading conditions, covering efficiency, voltage regulation, power transfer capability, and shunt current behavior.
3. Techno-economic comparison of the three transmission options, quantifying capital costs, loss-related costs, and component sizing for a representative Colombian offshore wind project.
4. Identification of operational advantages of LFAC over HVAC in medium-distance submarine–overhead hybrid routes, and its cost advantages over HVDC for the studied case.

1.4. Organization of the Paper

The remainder of this paper is organized as follows: Section 2 details the technical and economic modeling framework, including transmission system configuration, control strategies, performance evaluation metrics, and cost estimation methodology. Section 3 presents the simulation of the LFAC solution and cost analysis outcome comparison with HVAC, and HVDC alternatives. Section 4 interprets these results in light of existing literature, outlines study limitations, and discusses implications for future offshore wind integration in Colombia, concluding with a synthesis of the main findings and contributions.

2. Methodology

The evaluation of the proposed LFAC transmission system followed an integrated approach combining electrical design, geographic routing, dynamic simulation, and cost analysis. The methodology begins with the identification and modeling of the transmission route, covering both submarine and overhead segments. It then describes the electrical design of the transmission infrastructure, including conductors, transformation equipment, and substations, followed by the configuration of the back-to-back modular multilevel converter (MMC) for frequency conversion between 20 Hz and 60 Hz. Subsequently, the modeling and simulation procedures used to assess steady-state and dynamic performance are detailed. Finally, the framework for the techno-economic comparison with HVAC and HVDC alternatives is presented.

The overall methodological workflow adopted in this study is summarized in Figure 1. The process begins with the definition of project inputs, followed by the design of the LFAC system, model implementation, and subsequent technical and economic evaluations. Finally, a comparative assessment with HVAC and HVDC alternatives is carried out to determine the feasibility of the proposed solution.

Figure 2 provides an overview of the proposed transmission architecture, showing the offshore wind farm, the submarine and overhead segments, the transition substation, the frequency conversion station, and the interconnection with the National Interconnected System (SIN for its acronym in spanish) at Sabanalarga substation.

2.1. Transmission Line Routing

The routing of the transmission system was determined through a multi-criteria spatial analysis using a weighted-overlay procedure in a geographic information system (GIS), encompassing both the submarine and overhead segments. Figure 3 summarizes the routing results, depicting the integrated overhead and submarine routes in a three-dimensional environment. The submarine route extends from the offshore wind farm site at 10° 2’ 13.75" N, 75° 34’ 21.05" W to the transition substation on the mainland (10° 51’ 58.93" N, 75° 6’ 5.89" W). By contrast, the overhead route connects the transition substation to the interconnecting substation (Sabanalarga substation), located at 10° 38’ 55.68" N, 75° 54’ 38.36" W.

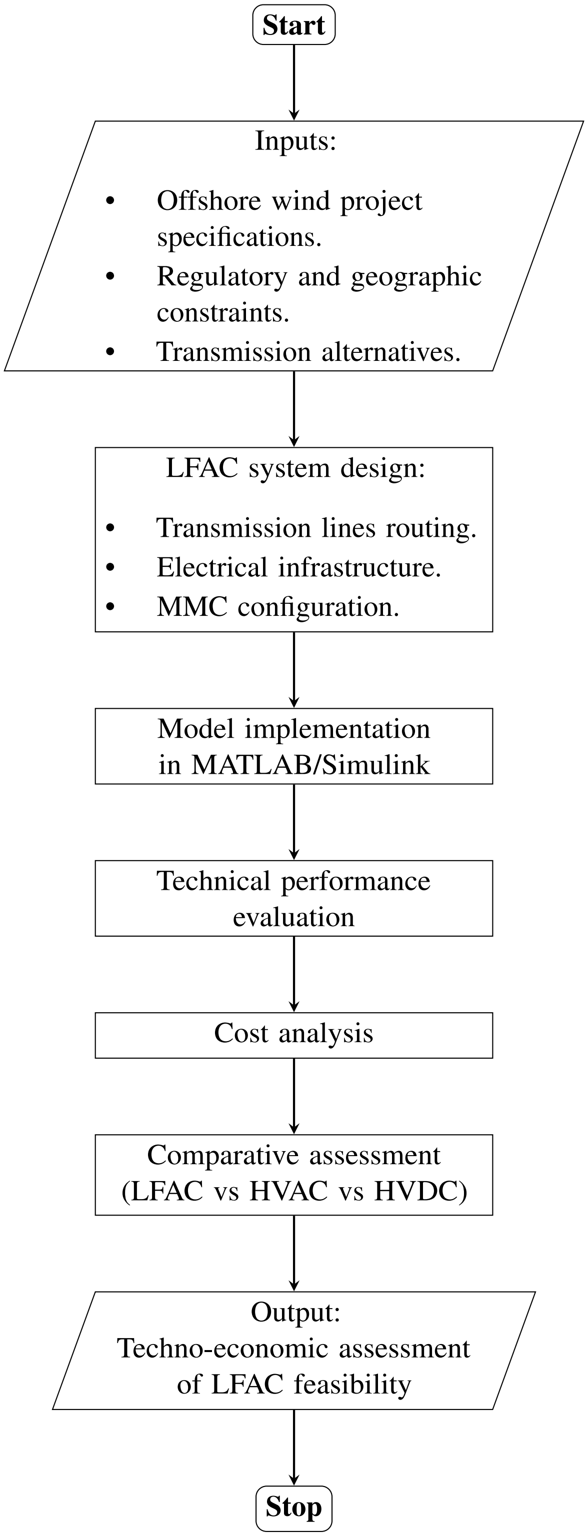

Figure 1. Flowchart of the methodology used for the techno-economic assessment of the proposed LFAC transmission system.

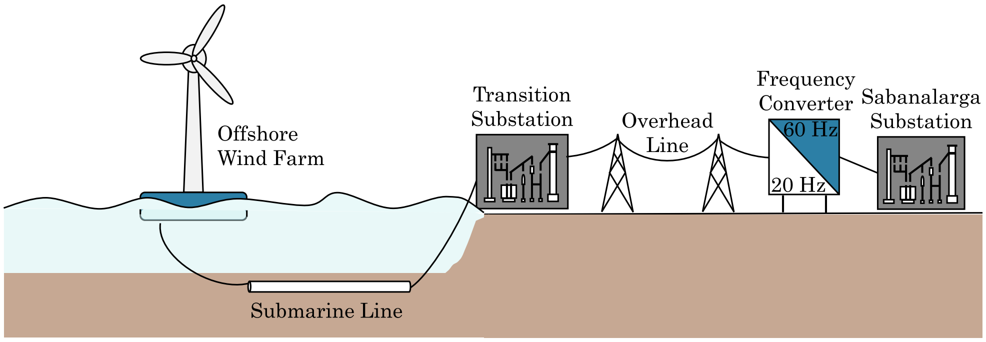

Figure 2. Typical LFAC transmission scheme for offshore wind farm integration.

Figure 3. Final transmission route visualized in Google Earth, including both overhead and submarine, and their coordinates.

This visualization allows the identification of technical constraints along the route, such as the maximum terrestrial elevation, which is critical for conductor clearance, thermal rating, and installation planning.

2.2. Electrical Design of the Transmission Infrastructure

This section introduces the overall electrical design of the transmission infrastructure developed for the offshore integration project, comprising a 75 km submarine segment, a 34 km overhead segment, and a transition substation. The design work focuses exclusively on electrical dimensioning-conductor selection, parameter calculation, and compliance with relevant technical standards—while mechanical aspects (e.g., structural loading, tower mechanics, or civil works) are intentionally excluded at this stage. A back-to-back modular multilevel converter (BtB–MMC) enables frequency conversion between the 20 Hz LFAC link and the 60 Hz grid; given its central role, the BTB–MMC is presented separately in Section 2.3.

2.2.1. Submarine Transmission

The submarine segment consists of two parallel three-core XLPE-insulated cables, each rated at 220 kV with a copper conductor cross-section of 1000 mm^2. This configuration was selected after evaluating alternatives such as three single-core cables. The three-core option was ultimately preferred due to its lower installation cost, smaller electromagnetic footprint, and reduced seabed occupation, while maintaining thermal and electrical reliability [14].

Each cable (3×1000 mm^2) includes a lead sheath, steel wire armor, and a polyethylene outer jacket, as summarized in Table 1, following the design guidelines in CIGRÉ Technical Brochure 880 [15].

Table 1. Main specifications of the submarine cable [15].

Parameter	Value
Rated Voltage	220 kV
Conductor Material	Compacted round copper
Conductor Cross-section	1000 mm^2
Insulation Material	XLPE
Insulation Thickness	23.0 mm
Lead Sheath Thickness	3.6 mm
Armor	133 stainless steel wires, 5.0 mm diameter
Outer Diameter	245 mm
Cable Weight	113 $\mathrm{kg\,m^{-1}}$

The ampacity was calculated according to IEC 60287 [16] and the CIGRÉ TB 880 [15] case study, using the thermal resistance method. The following installation and environmental conditions were applied:

- Seabed thermal resistivity: 0.7 $\mathrm{K\,m\,W^{-1}}$ (predominantly sandy with some silt) [17].
- Ambient seabed temperature: 11 °C, derived from surface temperature and thermal gradients at 1000 m depth [18].
- Cable burial depth: 1 m, for protection against anchors and bottom trawling [19].

The maximum conductor operating temperature was set to 90 °C. Skin and proximity effects were corrected for 20 Hz operation, and losses in dielectric insulation, metallic sheath, and armor were included. The continuous current-carrying capacity obtained was 1271.8 A per cable.

For the total transmission capacity of 960 MW at 220 kV, each cable carries 480 MW, equivalent to approximately 1254 A—well within the thermal limit. A separation distance of 3 km between the two cables was adopted to minimize thermal and electromagnetic coupling, exceeding the 2–3× water depth recommendation (about 1007 m) [20].

Positive- and zero-sequence impedance and admittance values were calculated following the CIGRÉ B1-10693 [21] methodology, adjusted for 20 Hz operation. These were used to derive the parameters of the π-equivalent model, expressed as distributed resistance, inductance, and capacitance per unit length for implementation in the Simulink transmission line block. The resulting values are presented in Table 2.

Table 2. Positive- and zero-sequence parameters of the submarine transmission line.

	Zero Sequence	Positive Sequence
Resistance (mΩ/km)	12.806	94.343
Inductance (μH/km)	195.10	342.63
Capacitance (nF/km)	380.20	37.998

2.2.2. Overhead Transmission

The overhead segment of the transmission system spans 34 km and operates at 220 kV and 20 Hz. Figure 4 presents the tower configuration adapted from the 230 kV transmission line manual published by the Electric Power Research Institute (EPRI) [22]. This arrangement defines the relative positions of phase conductors and shield wires, influencing electromagnetic performance, insulation coordination, and lightning behavior.

The selected phase and shield conductors are described in Table 3. The phase conductors correspond to ACSR Bittern (1272 kcmil, diameter 34.16 mm, weight 2139 kg km^{-1}), configured as a triple bundle, while the shield wires are Alumoweld 7#10 (diameter 7.76 mm, weight 245.1 kg km^{-1}).

Table 3. Specifications of the selected phase conductors and shield wires.

Phase conductor (ACSR Bittern)		**Shield wire (Alumoweld 7#10)**	
Material	Aluminum, ACSR	Material	Alumoweld
Gauge	1272 kcmil	Diameter	7.76 mm
Diameter	34.16 mm	Weight	245.1 kg km^{-1}
Weight	2139 kg km^{-1}	DC Resistance (20°C)	2.33 Ω km^{-1}
AC Resistance (75°C)	0.056 Ω km^{-1}	Breaking load	4.55 kN
DC Resistance (20°C)	0.044 Ω km^{-1}	Radius	3.88 mm
Breaking load	15 461 kg	RMG’	3.02 mm
Radius	17.08 mm		
RMG’	13.30 mm		
Current capacity	1183 A		
Number of bundles	3		

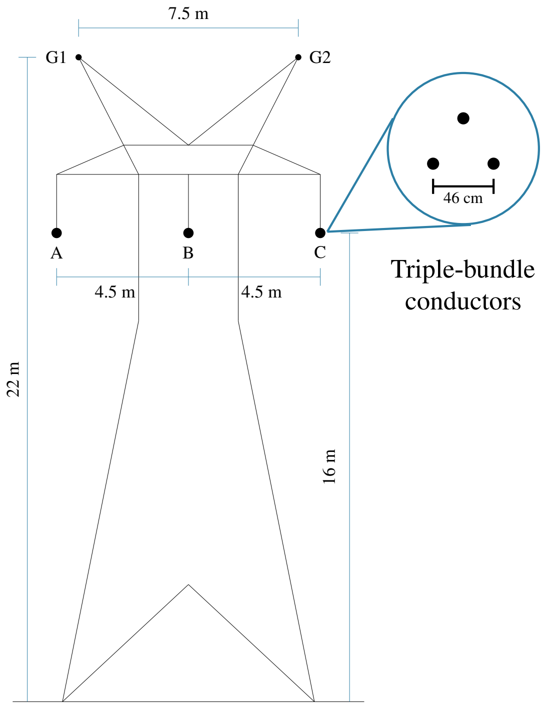

Figure 4. Arrangement of phase conductors and shield wires on the tower.

Performance verification included four main aspects:

- **Thermal performance:** Ampacity, calculated according to IEEE Std 738 [23], was 865.4 A, exceeding the nominal current of 839.8 A, ensuring safe thermal operation.

- **Corona inception:** The peak electric field on the conductor surface was below the breakdown strength of air, indicating no corona effects under nominal conditions.
- **Short-circuit withstand:** The conductor's thermal limit during faults was verified, with a calculated withstand current of 110.1 kA, confirming adequate short-term thermal capacity.
- **Electromagnetic fields:** Computed along the right-of-way, both electric and magnetic fields were below the limits stipulated by the Technical Regulations for Electrical Installations (RETIE for its acronym in spanish), ensuring compliance with Colombian safety regulations [24].

For shielding, the thermal behavior of the Alumoweld 7#10 under fault conditions was evaluated using short-circuit currents from DIgSILENT simulations and the method in [25], resulting in a peak temperature of 193.96 °C.

Finally, the positive- and zero-sequence parameters were derived from impedance and admittance matrices for 20 Hz operation, as shown in Table 4. These were used to model the line as a π-equivalent in Simulink for dynamic simulations.

Table 4. Positive- and zero-sequence parameters of the overhead transmission line.

	Zero Sequence	**Positive Sequence**
Resistance	21.8 mΩ/km	18.7 mΩ/km
Inductance	2.6 mH/km	0.7 mH/km
Capacitance	4.36 nF/km	16.4 nF/km

2.2.3. Transition Substation

The transition substation was conceptually designed to interface the submarine and overhead transmission segments. Its design followed key international standards, including IEC 60071 [26] for insulation coordination, IEC 60038 [27] for voltage levels, IEC 60099 [28] for surge protective device (SPD) selection, and IEC 60815 [29] for minimum safety clearances. Table 5 summarizes the main insulation and surge protection parameters resulting from the design process.

Table 5. Summary of insulation and surge protection parameters for the transition substation.

Insulation Parameters			**SPD Parameters**		
Description	**Value**	**Unit**	**Description**	**Value**	**Unit**
Rated equipment voltage U_s	245	kV	Nominal discharge voltage U_r	185.65	kV
Short-duration withstand at power frequency	460	kV	Absorbed energy W'	316.91	kJ/kV
			Line discharge class	2	–
Lightning impulse withstand voltage	1050	kV	Lightning impulse residual voltage	580	kV
Minimum phase-to-phase clearance	2100	mm	Switching impulse residual voltage	386	kV
Minimum phase-to-earth clearance	1900	mm	–	–	–

2.3. Frequency Conversion Station

The 960 MW frequency conversion station of this study is a key component of the proposed LFAC system, facilitating interconnection between the offshore 20 Hz transmission link and the onshore 60 Hz grid. Early LFAC implementations employed cycloconverters, which were limited by poor waveform quality and high harmonic distortion. Advances in power electronics have led to the adoption of modular multilevel converters (MMCs), which offer high scalability, excellent waveform fidelity, and fully independent control on both sides of the system.

This project adopts a back-to-back (BtB) MMC [30] comprising two MMCs linked by a common DC bus. This configuration enables bidirectional active power exchange between asynchronous AC systems via the interconnecting DC link as depicted in Figure 5. Each MMC interfaces with its external network through six branches. Each branch comprises an inductor L_B and a series chain of hundreds of submodules that act as a controlled voltage source. Each submodule is typically a half-bridge capable of bidirectional current flow and unidirectional voltage synthesis.

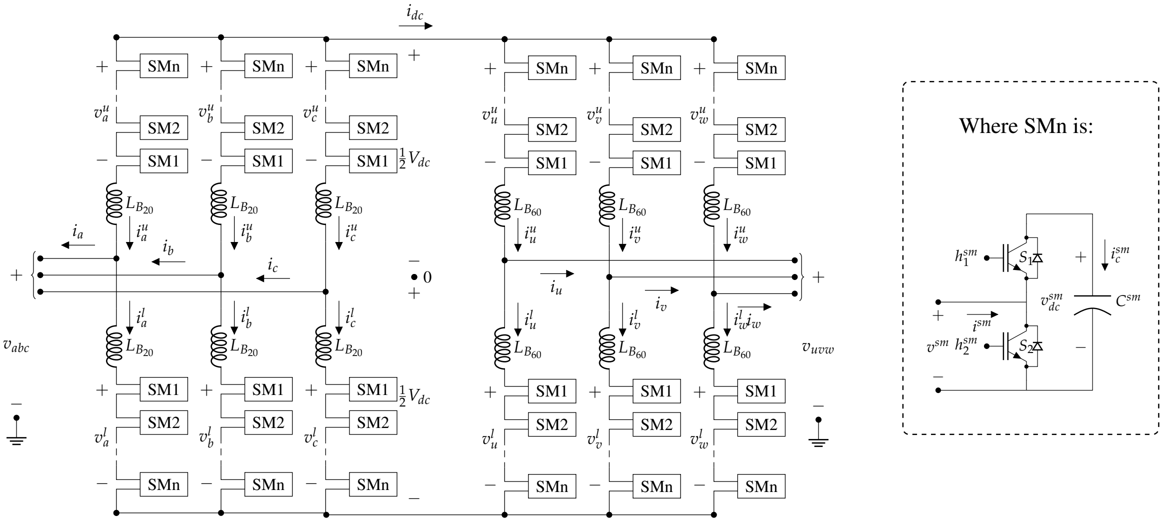

Figure 5. Back-to-back MMC model. Adapted from [31].

2.3.1. Selection of the Low Frequency

From an optimal-power-flow perspective, the LFAC operating frequency should be treated as a design variable rather than as a fixed assumption. In this line, the work in [32, 33] showed that the preferred frequency depends on the network topology and on the binding constraints of the LFAC corridor: decreasing frequency first relaxes angle-difference limits on stability-constrained lines, then leads to a thermally constrained region in which additional frequency reduction provides limited incremental benefit, and, at still lower frequencies, voltage-drop constraints become dominant.

For offshore wind integration, frequency selection is additionally governed by a techno-economic tradeoff. Lower frequency reduces charging current, reactive-power burden, and, in many cases, the number of cables required, whereas very low frequency increases transformer size and weight and, consequently, offshore-platform cost. This balance is explicit in the offshore-wind literature. The study [34] reported that frequencies below 20 Hz can achieve cost of energy comparable to VSC-HVDC, with optimum frequencies in the 17–13 Hz range for transmission distances between 100 and 200 km, while [35] showed that total LFAC cost reaches a minimum because cable-related costs increase with frequency whereas transformer/platform costs increase as frequency decreases.

Within that broader range, the selection of 20 Hz is also consistent with the conventional LFAC choice of approximately one-third of the rated grid frequency. In [35] is stated that most LFAC studies choose the operating frequency at 20/16.7 Hz. In the same line, the study in [36] concluded for a 1000 MW, 220 kV, 200 km offshore-wind case that the maximum admissible transmission frequency is 20 Hz and therefore selected 20 Hz as the final design value after considering both transmission capability and equipment realization.

2.3.2. Reactive Component Design

Following the methodology in [37], the arm inductances, series resistances, and submodule capacitances were sized to meet operating limits on both the 20 Hz and 60 Hz sides. The resulting design parameters are summarized in Table 6.

Additionally, to avoid overmodulation in the converter arms, the modulation index m was limited to 0.9, yielding the determination of the rated DC voltage of the conversion station:

$$V_{\mathrm{dc}} = \frac{2V_{B1,B2}}{m}, \tag{1}$$

where $V_{B1,B2}$ is the peak arm voltage.

Table 6. Steady-state design parameters of the back-to-back MMC for 20 Hz/60 Hz frequency conversion.

20 Hz Side		**60 Hz Side**		**Unit**
Parameter	**Value**	**Parameter**	**Value**	
Arm inductor $L_{B_{20}}$	2.0	Arm inductor $L_{B_{60}}$	6.0	mH
Arm resistance $R_{B_{20}}$	280	Arm resistance $R_{B_{60}}$	280	mΩ
DC-side values				
Arm capacitor C_S		977		μF
Capacitor voltage V_{dc}		402.8		kV

2.4. Model Implementation for Simulation and Analysis

To evaluate the dynamic behavior of the proposed transmission system, a comprehensive simulation model was developed in `MATLAB/Simulink`. The model integrates the key electrical components described in Sections 2.2 and 2.3 — including the overhead and submarine transmission lines, the modular multilevel converter — together with the associated control systems, under realistic operating conditions. Each block was built using average-value representations, with parameters extracted from detailed electrical analyses described in previous sections to ensure consistency between the design and simulation phases.

The complete Simulink model is shown in Figure 6, and served as the foundation for all simulations and performance assessments discussed in subsequent sections.

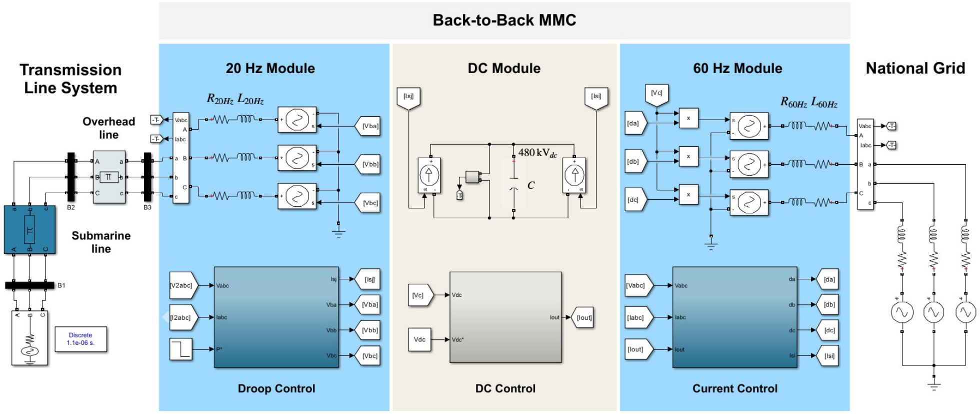

Figure 6. Complete Simulink model.

2.4.1. Transmission Line Modeling

The overhead and submarine transmission lines were modeled in Simulink using the π-equivalent circuit approach, based on previously calculated electrical parameters.

In the case of the submarine section, where two cables operate in parallel, the final model was obtained by computing the parallel combination of two identical π-circuits. This allowed the submarine segment to be represented by a single equivalent π-circuit, just like the overhead line.

This modeling strategy enables consistent integration of both segments into the dynamic simulation environment, ensuring accurate representation of line behavior under different operating conditions.

2.4.2. Power Conversion Modeling

The BtB-MMC depicted in Figure 5 is modeled using the simplified equivalent circuit shown in Figure 7, which captures active power transfer in AC/AC conversion. Unlike detailed switching models, this representation simplifies simulation while preserving the system's key dynamic behavior. It is particularly suitable for analyzing steady-state performance, low-frequency dynamics, control dynamics, and energy flow, while significantly reducing computational cost.

In the simplified equivalent circuit, each AC side of the converter is modeled as a controlled voltage source in series with an inductance ($L = \frac{1}{2}L_B$) and a resistance ($r = \frac{1}{2}R_B$). The lumped DC stage, which represents the total DC section of the converter, comprises an equivalent capacitor ($C = 6C_S$) in parallel with two DC current sources (i_{dcl} and i_{dcg}) that enable active power transfer through the DC link.

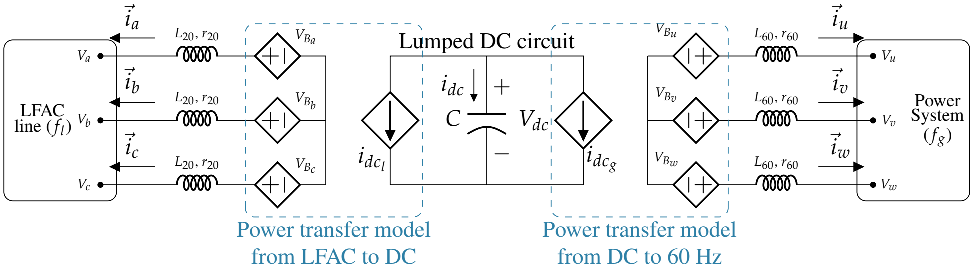

Figure 7. Averaged model of the MMC-BTB converter.

Active power transfer between the 20- or 60-Hz AC side and the DC side of the MMC follows the converter transfer relation in Equation 2. According to this relation, the AC phase voltages V_{Bx} are synthesized by modulating the DC voltage V_{dc} with the duty cycles d_{Bx}. Likewise, the DC currents i_{dcg} and i_{dcl} result from modulating the AC currents i_{abc} and i_{uvw}, respectively.

$$V_{Bx}(t) = d_{Bx}(t) \cdot V_{dc}(t), \quad x \in \{a, b, c, u, v, w\}, \tag{2a}$$

$$i_{dcl}(t) = \sum_{x=a,b,c} d_{Bx}(t) \cdot i_x(t), \tag{2b}$$

$$i_{dcg}(t) = \sum_{x=u,v,w} d_{Bx}(t) \cdot i_x(t). \tag{2c}$$

2.4.3. Power Conversion Control Modeling

The control of the converter is based on three objectives: (*i*) DC-voltage regulation, (*ii*) power-flow control on the 60 Hz side, and (*iii*) formation of the low-frequency network at the desired voltage magnitude and frequency. These three objectives are grouped into two control strategies. On the one hand, a Grid-Following control strategy with Phase-Locked Loop (PLL) is used on the 60 Hz side to regulate the

DC voltage and power flow via current control; on the other hand, a Grid-Forming control strategy with a Droop Control structure is implemented on the LFAC side to form the grid at 230 kV and 20 Hz.

Grid-Following Control in the 60 Hz side. The converter control on the 60 Hz side consists of two cascaded regulators in the rotating *dq* reference frame. The inner regulator controls the *d*- and *q*-axis currents (i_d and i_q) with a proportional (P) controller, and the outer regulator controls the DC voltage (V_{dc}) with a proportional-integral (PI) controller.

The inner current regulator, whose structure is given in Equation 3 and in Figure 8, provides the duty-cycle setpoints in the *dq* reference frame (d^*_{Bd} and d^*_{Bq}), which are then converted to the *abc* frame using the inverse Park transformation with the angle provided by the PLL. This regulator includes Disturbance Input Decoupling (DID) terms, represented by v_d and v_q, State Feedback Decoupling (SFD) terms for the *d*- and *q*-axis currents ($j\omega L$), and a proportional current regulator with gain K_{pii}.

$$d^*_{Bd} = \frac{v^*_{Bd}}{V_{dc}} = \frac{1}{V_{dc}}\left[v_d - \omega L i_q + K_{pii}(i^*_d - i_d)\right], \qquad d^*_{Bq} = \frac{v^*_{Bq}}{V_{dc}} = \frac{1}{V_{dc}}\left[v_q + \omega L i_d + K_{pii}(i^*_q - i_q)\right]. \tag{3}$$

The current references are derived from the active and reactive power commands (P^*_g and Q^*_g) and the *d*-axis terminal voltage (V_d), as given in Equation 4 and Figure 9.

$$i^*_d = \frac{2P^*_g}{3V_d} + \Delta i^*_d, \tag{4a}$$

$$\Delta i^*_d = K_{pv} \cdot (V_{dc} - V^*_{dc}) + K_{iv} \int_0^t (V_{dc} - V^*_{dc}(\tau))\, d\tau, \tag{4b}$$

$$i^*_q = -\frac{2Q^*_g}{3V_d}. \tag{4c}$$

However, the *d*-axis current command is adjusted through Δi^*_d to regulate the capacitor's DC voltage (V_{dc}) via the outer control loop with a PI regulator, in which V^*_{dc} is the voltage reference, V_{dc} is the measured DC voltage, and K_{pv} and K_{iv} are the controller gains.

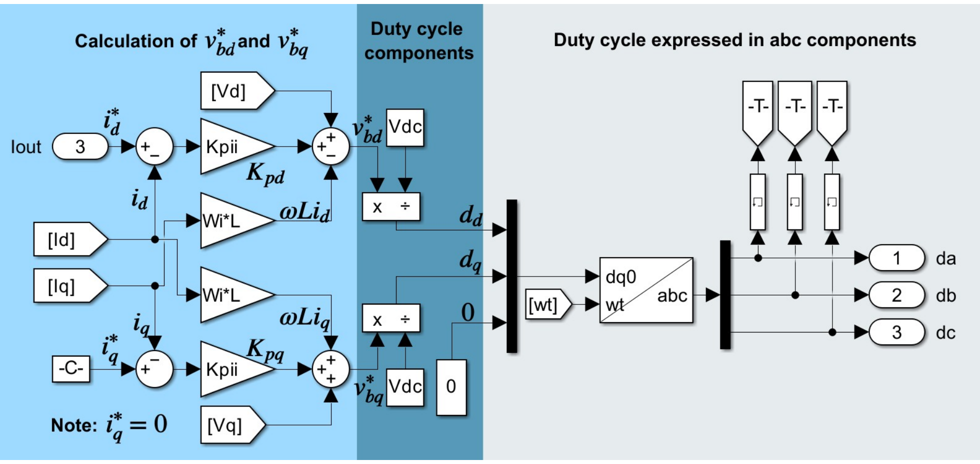

Figure 8. Simulink model of the current control system.

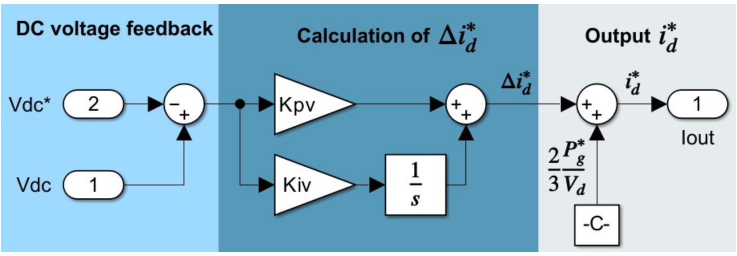

Figure 9. Simulink model of the DC voltage control system.

Grid-Forming Control in the 20 Hz side using Droop Relations. On the 20 Hz side of the BtB-MMC, a Grid-Forming control strategy is implemented. This allows the converter to operate as an autonomous voltage source on the low-frequency side, capable of establishing its own voltage and frequency references without relying on an external grid. Such an approach is particularly effective in LFAC systems, where weak grid conditions or islanded operation may arise. The implemented Grid-Forming control structure consists of a single-loop Droop Control in the rotating dq reference frame as depicted in (5), where δ represents the phase shift of the internal voltages v_{Bu}, v_{Bv}, and v_{Bw} shown in Figure 7, ω_0 and V_0 are the rated frequency and voltage, P^* and Q^* are the active and reactive power commands, P and Q are the measured powers, m_p corresponds to the power-frequency droop gain in units of radians per second per megawatt, and m_q is the reactive power-voltage drop gain in volts per megavar.

$$\frac{d}{dt}\delta = \omega - \omega_0 = m_p \cdot (P^* - P), \qquad V - V_0 = m_q \cdot (Q^* - Q). \tag{5}$$

In this control scheme, the converter frequency (ω) is regulated around the rated value (ω_0) through the active power flow in the transmission line. Likewise, the active power is controlled through the rate of change of the voltage angle ($d\delta/dt$) represented by the expression $m_p(P^* - P)$. On the other hand, (5) also shows that the voltage at the converter's terminals (V) is regulated through the reactive power flow and the droop gain m_q.

The full implementation of the grid-forming droop controller in Simulink is shown in Figure 10, which reflects the complete voltage and frequency regulation logic described above.

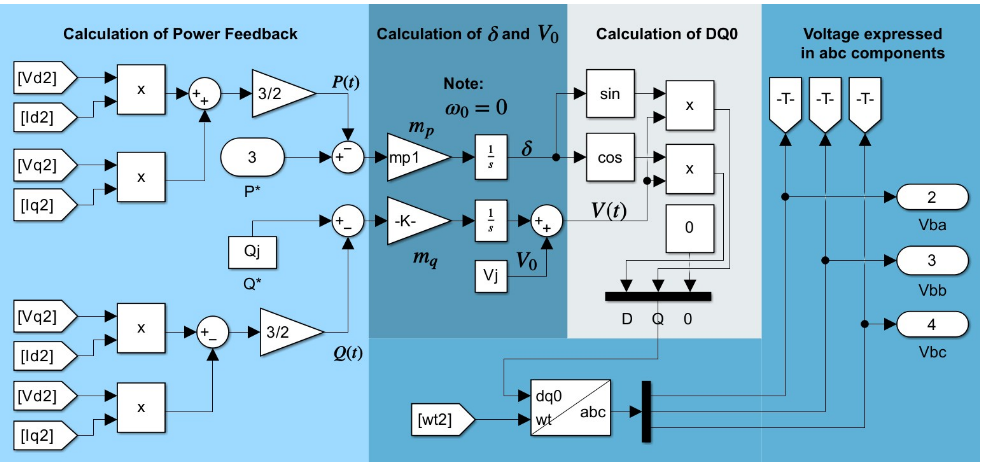

Figure 10. Simulink model of the Droop control system.

Using the methodology in [38] to compute the inner current and outer DC-voltage regulator gains, and the procedure in [39] to determine the droop gain m_p, the controller gains used in the simulations were obtained and summarized in Table 7.

Table 7. Summary of controller gains.

Grid-Following Control (60 Hz)						**Grid-Forming Control (20 Hz)**		
Inner Current Regulator			**Outer DC Voltage Regulator**			**Droop Control**		
Gain	**Value**	**Unit**	**Gain**	**Value**	**Unit**	**Gain**	**Value**	**Unit**
K_{pii}	6.3	Ω	K_{pv}	0.46	S	m_p	9.7	mrad/s/MW
K_{iii}	–	–	K_{iv}	25.0	S/s	m_q	0	kV/MVAR

2.4.4. Offshore Wind Farm Modeling and Operating Conditions

The offshore wind farm is modeled as an aggregated generation source with a rated capacity of 960 MW, connected to the transmission system at 220 kV and operating at 20 Hz on the LFAC side. The generation profile is assumed to be variable to represent wind intermittency, and simulations are conducted under different load factors ranging from partial to full-load conditions. The wind farm is represented using an equivalent power injection model, without detailed turbine-level dynamics, which is sufficient for system-level performance assessment. A unity power factor is assumed at the point of connection, and balanced three-phase operation is considered throughout the analysis.

2.5. Cost Analysis

This section describes the cost analysis (CA) framework used to evaluate transmission alternatives, including the cost models, nomenclature, and corresponding formulas. The cost analysis follows the approach outlined in [13], decomposing total project cost into terminal and route components (CAPEX) and their associated loss costs (OPEX) over the project lifetime.

2.5.1. Nomenclature and Parameters of the Cost Model

This subsection compiles the acronyms, constants, and variables employed in the CA assessment, ensuring clarity and consistency in the cost evaluation process. Tables 8–10 present these elements in detail: Table 8 lists the acronyms used throughout the analysis, Table 9 summarizes the constant parameters, and Table 10 defines the variables used in the cost model.

Table 8. Acronyms used in the economic assessment.

Acronym	Meaning	Acronym	Meaning
TCC	Terminal Capital Costs	CPC	Compensation Cost
RCC	Route Capital Cost	TLC	Terminal Power Losses Cost
CBC	Cable Cost	RLC	Route Losses Cost

Table 9. Constants adopted in the cost model.

Symbol	Description	Value / Unit
B_T	Base cost for HVAC offshore platform and plant	6.4 MUSD
C_T	Variable cost for HVAC platform and plant	0.058 MUSD/MVA
E	Average energy price	50 USD/MWh
F	Adjusted power factor	1.0 (–)
T_p	Project time	30 years
ε_{op}	Operation factor	0.231 (–)
f_T	Cost factor for transformer/converter per platform	0.2 (–)

Table 10. Variables used in the cost model.

Symbol	Description	Unit
n_T	VSC–HVAC converter number per platform	–
S_{TT}	Power transfer rating	MVA
c_c	Subsea cable cost per set (supply+install)	kUSD/km
l_c	Subsea cable length	km
n_c	Number of parallel subsea cable circuits	–
V_{cn}	Subsea cable nominal voltage	kV
f_n	Operating frequency	Hz
C	Subsea cable shunt capacitance per km	F/km
η_{off}	Offshore LFAC transformer efficiency	–
r_c	Subsea cable resistance per km	Ω/km

2.5.2. Cost Component Formulas

Unless otherwise stated, monetary results are expressed in MUSD; lengths in km; power in MVA; voltages in kV.

Terminal Capital Costs (TCC).

$$TCC_{\text{offLFAC}} = \sqrt{3}\, B_T \; + \; \left[1 + f_T\, n_T^2\right] \sqrt{3}\, C_T\, S_{TT}.$$

The factor $\sqrt{3}$ accounts for the three-phase basis as in [13]. When adapting HVAC cost bases to LFAC, frequency-related adjustments follow the same reference.

Route Capital Cost (RCC).

$$RCC_{\text{LFAC}} = CBC + CPC \qquad \text{with,} \quad \begin{aligned} CBC &= c_c \cdot l_c \cdot n_c, \\ CPC &= k_{\text{comp}}\, V_{cn}^2\, (2\pi f_n)\, C\, l_c. \end{aligned}$$

where k_{comp} is a proportionality coefficient (dimensioned to produce MUSD); when $k_{\text{comp}} = 0.02$ is used, explicitly state the unit convention for V_{cn} (kV) and C (F/km) to keep the consistency of the dimensions.

Terminal Loss Cost (TLC).

$$TLC_{\text{LFAC}} = S_{TT}\, F\, \left(1 - \eta_{off}\right) T_p\, \varepsilon_{op}\, E.$$

Route Loss Cost (RLC).

$$RLC_{\text{LFAC}} = \left(\frac{S_{TT}\, F\, \eta_{off}}{V_{cn}} \right)^2 r_c\, l_c\, n_c\, T_p\, \varepsilon_{op}\, E$$

Unit note: Use V_{cn} in kV consistently with S_{TT} in MVA to keep the current term in kA; otherwise convert explicitly.

2.5.3. Regulatory UC Update (CREG 015/2018)

For interconnection assets of the Colombian National Interconnected System (SIN) valued through Construction Units (UC) expressed in 2017 prices, the update to 2025 is calculated as:

$$\text{UC}_{2025} = \text{UC}_{2017} \times \frac{\text{PPI}_{2025}}{\text{PPI}_{2017}}$$

Alternatively, if annual Producer Price Index (PPI) values are used, the update factor shall be obtained by multiplying the corresponding yearly ratios. The source of the PPI must be stated, indicating whether the values correspond to index levels or accumulated factors.

3. Results

This section presents the technical and economic outcomes derived from the proposed hybrid LFAC transmission concept, benchmarking its performance against conventional HVAC and HVDC alternatives. The analysis covers voltage imbalance, end-to-end efficiency, and power transfer capability over mixed submarine–overhead routes, followed by a detailed techno-economic assessment. All results are based on the study parameters and methodology outlined in Section 2, ensuring consistent assumptions across performance and cost comparisons.

3.1. Control Validation and Dynamic Performance

The dynamic performance of the BtB-MMC was evaluated through time-domain simulations under varying operating conditions. The Grid-Forming operating mode at 20 Hz, employs an active-power droop controller that stabilizes power oscillations following load changes, as shown in Figure 11.

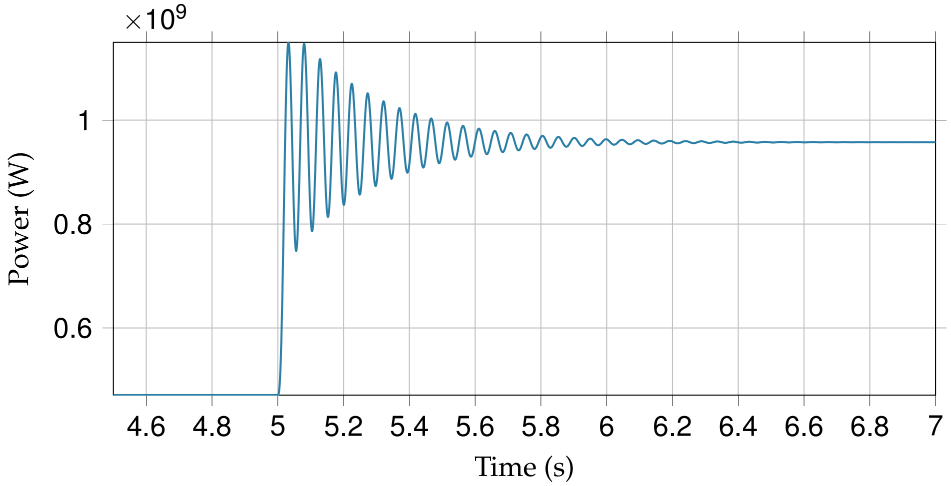

Figure 11. Response of the 20 Hz droop controller to step changes in active-power demand.

The Grid-Following operating mode at the 60 Hz side regulates the DC voltage as shown in Figure 12. The PI controller maintains the DC voltage within a ±2% band around its reference, even under sudden active-power setpoint variations, ensuring stable operation of the intermediate conversion stage. Finally, on the 60 Hz side, a decoupled current-control loop adjusts the injected current to track the demanded active and reactive power. Figure 13 shows accurate reference tracking with stable dynamic behavior.

These results confirm the technical feasibility of the MMC-based transformation station for LFAC applications in offshore wind farm integration.

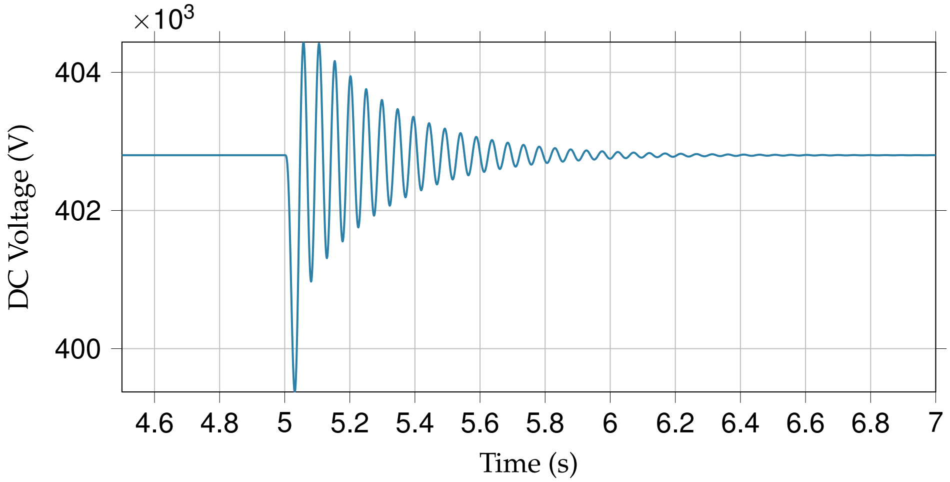

Figure 12. DC voltage regulation under active-power transients.

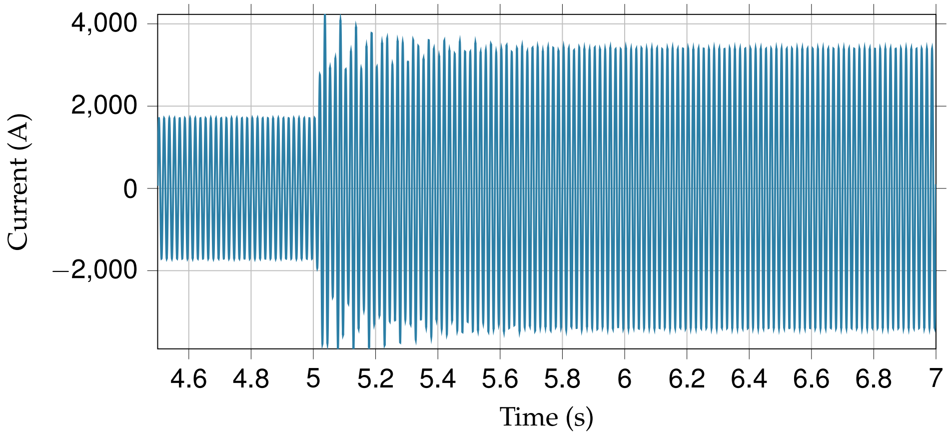

Figure 13. Current-control performance on the 60 Hz grid side.

3.2. Voltage Regulation and Negative-Sequence Imbalance

Voltage regulation was assessed by comparing the receiving-end voltage under no-load and full-load conditions, using:

$$\text{Regulation (\%)} = \frac{V_{\text{no-load}} - V_{\text{full-load}}}{V_{\text{full-load}}} \times 100, \tag{6}$$

where $V_{\text{no-load}}$ is the receiving-end voltage with no load applied, and $V_{\text{full-load}}$ is the voltage under nominal load.

As shown in Figure 14, regulation values ranged from 1.02% to 4.69%, remaining well below the 10% limit established by CREG 025 of 1995 [40].

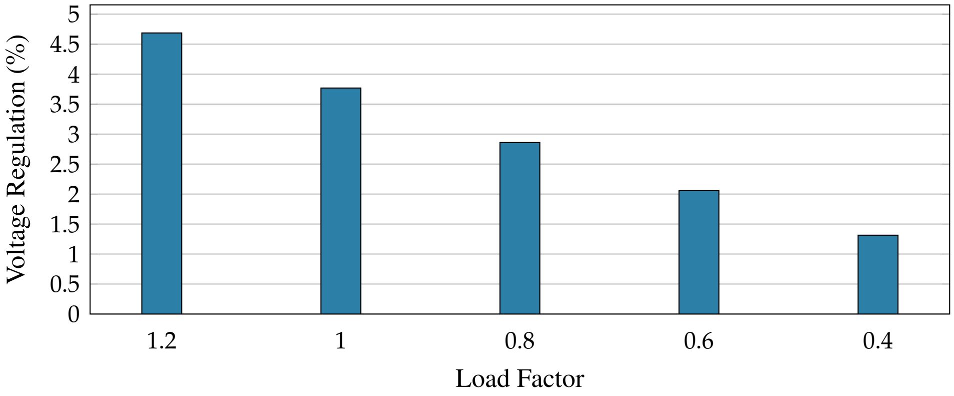

Figure 14. Voltage regulation for selected load factors.

Voltage imbalance was quantified through symmetrical component decomposition, according to:

$$\text{Imbalance } (\%) = \frac{|\tilde{V}_2|}{|\tilde{V}_1|} \times 100, \tag{7}$$

where $\tilde{V}_1$ and $\tilde{V}_2$ are the positive- and negative-sequence voltage components, respectively.

The calculated imbalance ranged from 0.0225% to 0.0233%, far below the 1.5% threshold defined by NTC 5001 [41] for voltages above 69 kV. These results, depicted in Figure 15, confirm excellent phase symmetry under all operating scenarios.

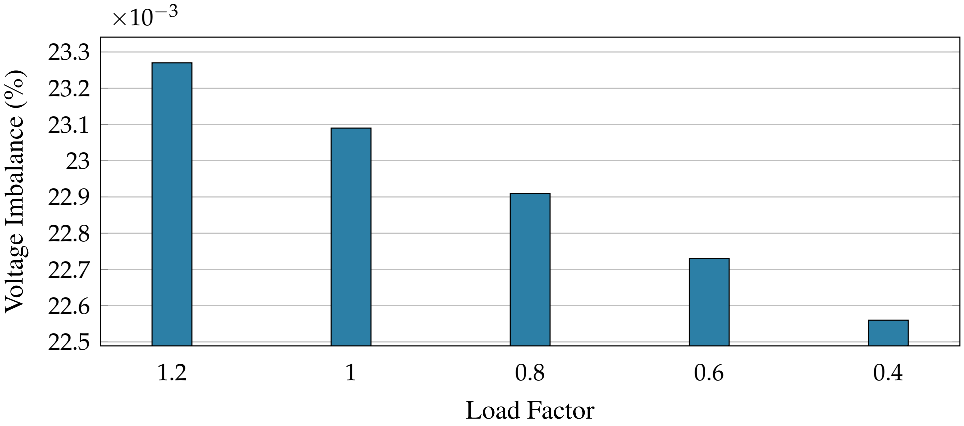

Figure 15. Negative-sequence voltage imbalance calculated from symmetrical components.

3.3. Capacitive Shunt (Charging) Currents

Capacitive shunt currents were obtained from the π-equivalent model of the transmission path. For each operating point, the shunt branch current phasor was computed as

$$\tilde{I}_{\text{sh}} = j\,\omega\,C\,\tilde{V}, \tag{8}$$

where $\tilde{I}_{\text{sh}}$ is the shunt-to-ground current phasor at each end of the line, $\tilde{V}$ is the node-voltage phasor, $\omega = 2\pi f$ is the angular frequency, and C is the equivalent shunt capacitance of the branch. Magnitudes are reported as $I_{\text{sh}} = |\tilde{I}_{\text{sh}}|$.

The calculation uses the network in Figure 16, which represents the complete π-equivalent of the mixed transmission path (submarine, *sub*, and overhead, *oh*). Each capacitive branch yields a local shunt current, $\tilde{I}_{\text{sh1}}$ through $\tilde{I}_{\text{sh4}}$, and the total shunt current is the sum of the four contributions:

$$\tilde{I}_{\text{sh,tot}} = \sum_{k=1}^{4} \tilde{I}_{\text{sh}k}. \tag{9}$$

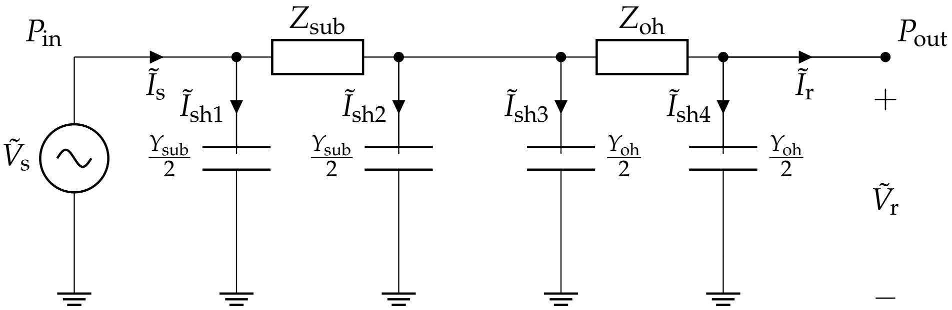

Figure 16. Mixed-path transmission model with π-type line representation (submarine and overhead segments).

As shown in Figure 17, shunt currents are markedly lower at 20 Hz (LFAC) than at 60 Hz (HVAC) for all load factors. The reduction is close to the theoretical ratio $60/20 = 3$, with LFAC currents being approximately 66% lower than HVAC. This follows directly from $Y_{\text{sh}} = j\omega C$, as the capacitive admittance is proportional to frequency. From a system perspective, this reduction in charging current decreases reactive power demand from the source, reduces voltage rise risk under light load, and lowers the required rating of shunt compensation devices. These benefits are particularly relevant in long submarine links, where charging current can limit transmission distance and operational flexibility.

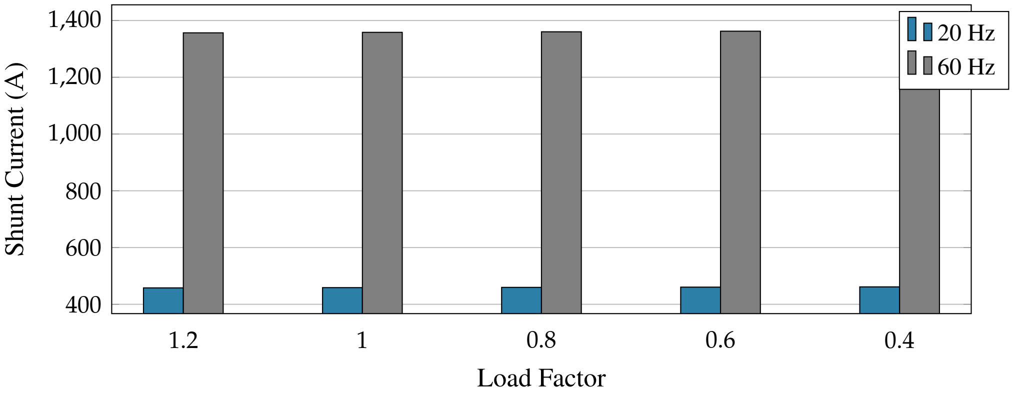

Figure 17. Capacitive shunt (charging) currents at 20 Hz and 60 Hz across load factors. Lower ω at 20 Hz reduces $|Y_{\text{sh}}|$ and thus the charging current, with LFAC showing a $\sim$ 66% reduction compared to HVAC.

3.4. End-to-End Efficiency vs. Load

The overall system efficiency was evaluated via simulations by computing the main loss components as follows:

$$\eta(\%) = \frac{P_{\text{out}}}{P_{\text{in}}} = 1 - \frac{P_{line} + P_{LB} + P_{cond} + P_{sw}}{P_{in}}, \tag{10}$$

where P_{out} and P_{in} denote the active power measured at the receiving and sending terminals, respectively; P_{line} represents transmission-line losses due to Joule heating; P_{LB} denotes the converter branch-inductor losses; P_{cond} represents the converter conduction losses; and P_{sw} denotes the converter switching losses.

Transmission-line and branch-inductor losses were obtained from simulations, whereas conduction and switching losses were computed assuming an ABB 5SHX 36LL4521 Reverse-Conducting IGCT [42] and using the analytical loss formulation presented in [37]. This loss-assessment procedure was applied across all simulated load levels, ensuring consistency with the efficiency results shown in Figure 18.

Under steady-state conditions (Load factor of 1.0), LFAC exhibits an efficiency of 94% with 6.0% losses. Approximately 3.0% (30 MW) is attributable to transmission-line losses, and an additional 3.0% (30 MW) is distributed roughly equally among branch-inductor, conduction, and switching losses.

As illustrated in Figure 18, the HVAC system exhibits slightly higher efficiency of about 1.0 to 1.5% higher compared to LFAC across all load levels. Despite the apparent advantage of HVAC, two points are salient. First, because charging currents in HVAC are higher, transmission-line losses are correspondingly higher than in LFAC for a given active power transfer. Specifically, at rated power transfer, simulations indicate that the HVAC system incurs 4.6% (44 MW) line losses, which is 50% higher than its LFAC counterpart. Second, the reduction in transmission-line losses in LFAC is offset by converter losses. The back-to-back MMC in the LFAC configuration introduces additional branch-inductor, conduction, and switching losses, which explains the observed decrease in efficiency. This behavior—where HVAC systems exhibit slightly higher efficiency than LFAC systems—aligns with previous reports [43] and can be regarded as a typical characteristic of such configurations. Furthermore, LFAC operation at 20 Hz inherently reduces capacitive charging currents and conductor losses, offering distinct advantages for medium-distance transmission.

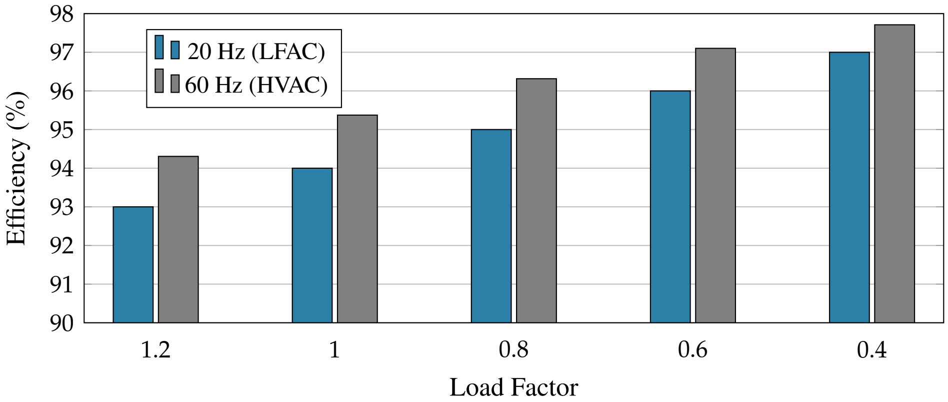

Figure 18. End-to-end efficiency comparison between LFAC (20 Hz) and HVAC (60 Hz) transmission systems under varying load factors.

3.5. Mixed-Path Power Transfer (20 Hz vs. 60 Hz)

Using the generalized three–phase power–transfer expression from Appendix A (symbols in Table A1), we evaluated $P = P(l, \delta, f)$ for the mixed submarine/overhead route. The model uses the study parameters for route fractions and per–unit–length inductances, comparing 20 Hz (LFAC) with 60 Hz (HVAC).

Figure 19 shows the resulting power–transfer surfaces. Key observations are:

- **Frequency effect:** For the same path and angle δ, the 20 Hz surface lies consistently above the 60 Hz surface. The theoretical gain factor from the inverse frequency term in P_{max} is $60/20 = 3$, which is closely reflected in the results (LFAC values ∼200% higher than HVAC).
- **Length and angle dependence:** For a fixed frequency, P decreases approximately as $1/l$ and increases with $\sin \delta$, peaking near $\delta \approx 90°$ in this lossless formulation.
- **Losses and shunt effects:** Including R and Y_{sh} would lower absolute maxima, but the relative advantage of LFAC over HVAC for medium distances remains robust for the studied route.

From a practical standpoint, the LFAC gain can extend the maximum deliverable power for a given route length, or alternatively allow operation at lower δ for the same transfer, improving angular stability margins. This is especially relevant for long submarine–overhead hybrids where inductive reactance limits power capability before thermal limits are reached.

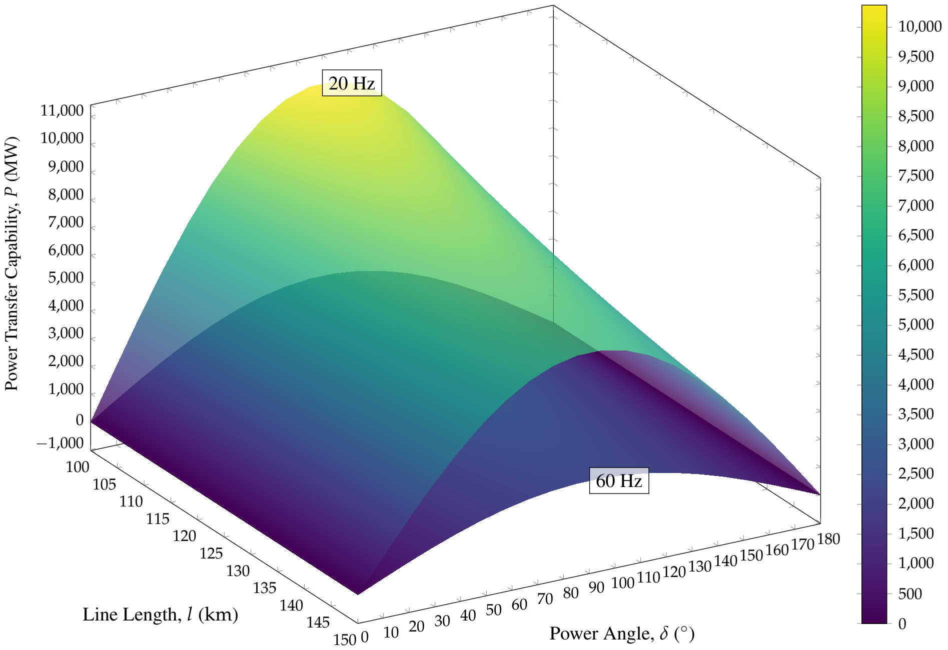

Figure 19. Maximum power transfer capability for 20 Hz and 60 Hz over the mixed submarine/overhead path. LFAC provides ∼200% higher capability for the same l and δ.

3.6. Techno-Economic Assessment

The cost evaluation was carried out following the methodology of [13] (Sec. 2.5), using the constants and variables defined above. Results are presented by project segment and benchmarked across HVAC, LFAC, and HVDC.

3.6.1. Offshore Segment (LFAC Option)

For the offshore portion of the LFAC alternative, the total investment is estimated at **405.61 MUSD**, broken down as:

- **Terminal Capital Costs (TCC):** 178.28 MUSD
- **Route and Cable Costs (RCC):** 213.36 MUSD (submarine cable and reactive compensation)
- **Terminal Loss Cost (TLC):** 6.16 MUSD
- **Route Loss Cost (RLC):** 7.82 MUSD

Figure 20 and Table 11 summarize the offshore cost structure for all technologies. Compared to HVAC, LFAC shows ∼9.4% higher offshore CAPEX, mainly due to more expensive terminals. However, it remains ∼8.1% below HVDC, which is dominated by high terminal costs despite its lower RLC.

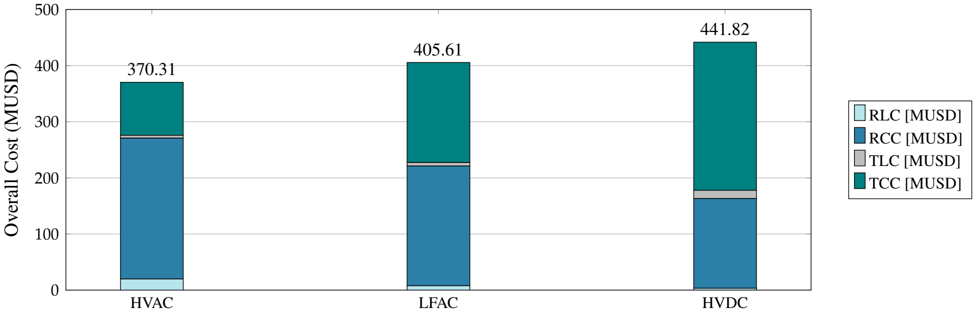

Figure 20. Cost breakdown of transmission system components per technology.

Table 11. Offshore cost breakdown by system: RLC, RCC, TLC, and TCC (MUSD).

System	RLC	RCC	TLC	TCC
HVAC	19.91	250.95	5.00	94.44
HVDC	3.35	159.77	14.71	263.98
LFAC	7.82	213.36	6.16	178.28

3.6.2. SIN Interconnection (CREG 015/2018 UCs, 2017→2025 PPI)

The onshore connection to the Colombian SIN (34 km overhead line, interconnection transformers, and transition substation) was costed using the CREG 015/2018 UC framework, updated from 2017 to 2025 by PPI. The total is **6.47 MUSD**, yielding a complete LFAC hybrid project cost of **412.08 MUSD**.

Table 12. Estimated cost for SIN interconnection components (updated UCs, CREG 015/2018).

Construction Unit (UC)	Cost [MUSD]
UC – Conductor, Guard Wire, and Tower	4.98
UC – STN Connection Transformers	1.32
UC – Transition Substation	0.165
Total	**6.47**

3.6.3. Cross-Technology CAPEX Comparison

Under the same assumptions, LFAC total CAPEX is 412.08 MUSD, ∼9.4% higher than HVAC (376.78 MUSD) but ∼8.1% lower than HVDC (448.29 MUSD). While LFAC entails higher upfront cost than HVAC, its technical benefits for medium distances—lower charging-current losses, reduced compensation needs, and simpler integration—may offset this gap in lifecycle cost analyses, particularly in submarine–overhead hybrid routes where HVAC's reactive limitations become critical.

3.6.4. Levelized Cost of Transmission and Sensitivity Analysis

To complement the CAPEX-based comparison and address uncertainties inherent in long-horizon infrastructure projections, this subsection introduces the Levelized Cost of Transmission (LCOT) as a normalized economic metric, and evaluates the sensitivity of the results to two primary cost drivers: the submarine cable unit cost (c_c) and the energy tariff (E).

Levelized Cost of Transmission.

The LCOT normalizes the total lifecycle cost of the transmission system by the total energy delivered over the project horizon, enabling a technology-neutral comparison on a per-MWh basis. Consistent with the undiscounted cost framework of Section 2.5, it is defined as:

$$\mathrm{LCOT} = \frac{\mathrm{TCC} + \mathrm{RCC} + \mathrm{TLC} + \mathrm{RLC}}{S_{TT} \cdot F \cdot T_p \cdot \varepsilon_{op} \cdot 8760}, \tag{11}$$

where the numerator aggregates the total capital (TCC, RCC) and loss-related (TLC, RLC) costs reported in Tables 11 and 12, and the denominator is the total energy transmitted over the project lifetime T_p, expressed in MWh. Using the parameters of Tables 9 and 10, the total delivered energy amounts to:

$$E_{\text{total}} = S_{TT} \cdot F \cdot T_p \cdot \varepsilon_{op} \cdot 8760 = 960 \times 1.0 \times 30 \times 0.231 \times 8760 \approx 58{,}279\ \mathrm{GWh}, \tag{12}$$

The resulting LCOT values for each technology are presented in Table 13.

Table 13. Levelized Cost of Transmission (LCOT) by technology.

Technology	Total Lifecycle Cost (MUSD)	E_{total} (GWh)	LCOT (USD/MWh)
HVAC	376.78	58,279	6.47
LFAC	412.08	58,279	7.07
HVDC	448.29	58,279	7.69

The LCOT confirms the relative cost ordering established by the CAPEX comparison: LFAC lies between HVAC and HVDC, with a normalized cost ∼9.2% above HVAC and ∼8.1% below HVDC. On an absolute basis, the gap between HVAC and LFAC amounts to 0.60 USD/MWh, and that between LFAC and HVDC to 0.62 USD/MWh. These modest differences reflect the dominant weight of capital expenditures across all three configurations, where loss-related costs (TLC + RLC) represent at most 6.6% of the total lifecycle cost.

Sensitivity Analysis.

Offshore transmission costs are inherently subject to market and regulatory volatility. To assess the stability of the LCOT ranking, two parameters were varied by ±30% from their base values while all other inputs were held constant: the submarine cable unit cost c_c, which enters through the cable cost component (CBC) of the RCC; and the energy tariff E, which scales the loss-related costs TLC and RLC proportionally. These parameters were selected because they represent the dominant cost drivers of the economic model, capturing the primary sources of uncertainty in capital expenditure (through cable costs) and operational expenditure (through energy pricing). Table 14 reports the resulting LCOT for each technology and scenario, and Figure 21 illustrates the variation across both parameters for all three technologies.

Table 14. LCOT sensitivity (USD/MWh) to ±30% variation in cable unit cost (c_c) and energy tariff (E).

Parameter	Scenario	HVAC	LFAC	HVDC
	−30%	5.18	5.97	6.87
Cable cost c_c	Base	6.47	7.07	7.69
	+30%	7.75	8.17	8.52
	−30%	6.34	7.00	7.60
Energy tariff E	Base	6.47	7.07	7.69
	+30%	6.59	7.14	7.78

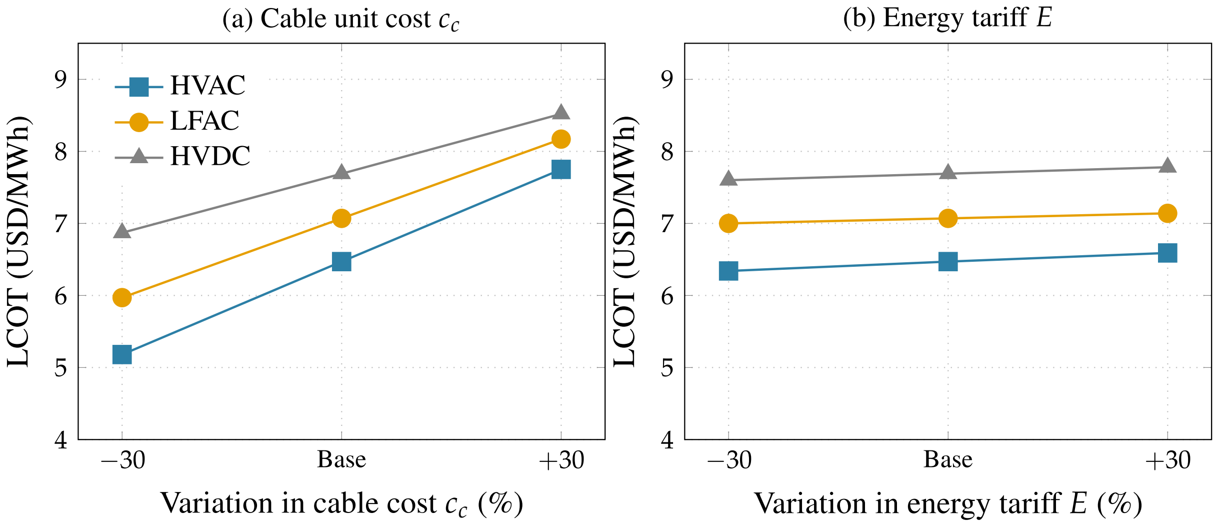

Figure 21. Sensitivity of LCOT to ±30% variation in (a) submarine cable unit cost c_c and (b) energy tariff E.

Two principal findings emerge from the sensitivity analysis in Figure 21. First, cable unit cost is the dominant uncertainty driver across all technologies: a ±30% variation in c_c shifts the LCOT of HVAC, LFAC, and HVDC by ±1.29, ±1.10, and ±0.82 USD/MWh, respectively — an effect roughly 15 times larger than that of the energy tariff (±0.13, ±0.07, and ±0.09 USD/MWh for the same technologies). This asymmetry directly reflects the capital-intensive structure of offshore transmission. Second, the relative ordering HVAC $<$ LFAC $<$ HVDC is preserved across all tested scenarios, including the extreme case of cable costs falling by 30%, confirming that the economic positioning of LFAC is robust to realistic cost uncertainty. Notably, HVAC exhibits the greatest sensitivity to cable cost fluctuations, owing to its higher RCC (250.95 MUSD vs. 213.36 MUSD for LFAC), which implies that future reductions in submarine cable prices would benefit HVAC proportionally more — reinforcing, rather than undermining, LFAC's intermediate positioning.

4. Discussion

The results presented in Section 3 demonstrated clear technical and economic differences between the evaluated transmission alternatives. In this section, these findings are analyzed in detail, relating them to previous studies, identifying their practical implications for the Colombian context, and highlighting the main contributions of this work. The discussion also addresses the study's limitations, outlines potential directions for future research, and concludes with a synthesis of the key messages for stakeholders and decision-makers.

4.1. Interpretation of Results and Relevance

The simulation outcomes confirm several advantages of the proposed 20 Hz LFAC configuration over conventional 60 Hz HVAC links for medium-distance offshore wind transmission in the Colombian Caribbean context. These advantages align with, and in some cases expand upon, the trends reported in previous LFAC feasibility studies conducted in other regions.

First, the measured reduction in submarine cable charging currents—approximately 66% compared to HVAC—is consistent with the theoretical frequency ratio ω_{60}/ω_{20} and with empirical findings from [10, 12], where charging current magnitude was shown to scale linearly with frequency. This reduction not only minimizes reactive power demand, as also highlighted by [11], but also extends the technically feasible length of AC submarine links without requiring intermediate compensation.

Second, the observed improvement in power transfer capability—approximately 200% higher than HVAC for the same route length and load angle—is in line with the inverse frequency dependence of P_{max} described in [7] and demonstrated experimentally in [12]. For the Colombian case, this margin can translate into either higher deliverable offshore capacity or improved angular stability when operating below thermal limits.

Third, the slightly lower efficiency of LFAC is mainly attributable to additional converter losses that diminish the reduction in transmission-line losses achieved by lowering charging currents. However, deploying advanced MMC topologies, such as the Hybrid MMC (HMMC) recently proposed in [44], can markedly reduce semiconductor and capacitor losses. Experimental and analytical results show that the best-performing HMMC configuration achieves up to 32% lower total power losses and approximately 30% fewer devices than a conventional MMC, thereby improving both power density and efficiency at medium- and high-voltage levels.

From a regulatory compliance standpoint, the LFAC design meets the CREG 025/1995 voltage regulation limit of ±10% and the NTC 5001 voltage unbalance limit of 1.5% for voltages above 69 kV. These performance levels are comparable to the European LFAC pilot systems discussed in [11], reinforcing the technology's readiness for deployment under existing Colombian grid codes.

Economically, while our LFAC configuration shows a 9.4% higher CAPEX than HVAC, it remains 8.1% below HVDC for the same point-to-point connection. This positioning is consistent with the cost-distance trends established in [4, 13], where LFAC is shown to be competitive in the 80–200 km range, particularly for capacities in the several-hundred-megawatt scale. Given the medium distances and combined submarine–overhead topology of the studied route, the LFAC option emerges as a technically robust and economically viable alternative for Colombia's first offshore wind interconnections. This conclusion is further supported by the LCOT results, which indicate that the cost difference between LFAC and HVAC remains relatively small (on the order of 0.6 USD/MWh), despite the significant technical advantages offered by LFAC in terms of power transfer capability and reduced charging currents. Moreover, the sensitivity analysis confirms that this economic positioning is robust under realistic variations in key cost drivers, with submarine cable cost emerging as the dominant factor while preserving the relative ranking of the evaluated technologies.

In summary, the present work not only corroborates the technical and economic patterns identified in international LFAC research, but also extends their validation to the Colombian regulatory, geographic, and resource context. This positions LFAC as a compelling transmission option to support the large-scale integration of offshore wind in Colombia, bridging the gap between HVAC's technical limitations and HVDC's high upfront costs.

4.2. Study Limitations

The analysis presented in this work is subject to several technical and methodological limitations that should be considered when interpreting the results.

First, the electrical assessment was carried out under nominal operating conditions and selected load-change scenarios, but it did not include a detailed evaluation of severe system contingencies. Events such as short circuits in the submarine or overhead sections, converter blocking, transformer energization, protection maloperation, temporary overvoltages, or post-fault restoration were not explicitly modeled. Therefore, although the results support the technical feasibility of the proposed LFAC scheme under normal operation, additional contingency-oriented studies are still required to assess its behavior under abnormal and faulted conditions.

Second, the study was developed for a representative design case and does not constitute a full sensitivity analysis of all influential variables. Only sensitivity analysis on the economical evaluation was performed. However, parameters such as transmission distance, cable capacitance, thermal resistivity, conductor sizing, loss coefficients, energy price, and project lifetime were fixed according to the selected scenario. Likewise, the design comparison was performed with a single LFAC operating frequency and voltage level. Variations in these assumptions could modify the relative technical and economic performance of LFAC, HVAC, and HVDC alternatives.

Third, several design parameters were intentionally fixed to maintain a tractable comparison framework. The study does not explore alternative converter topologies, different numbers of parallel submarine circuits, or broader frequency-selection optimization beyond the adopted 20 Hz case. As a result, the reported efficiency, power-transfer capability, and cost values should be interpreted as scenario-specific rather than universally generalizable.

Finally, the economic and geographic assessments remain at a conceptual level. The cost analysis includes capital expenditure and simplified loss-related operating costs, but excludes detailed treatment of long-term O&M, financing structure, technology learning effects, and supply-chain uncertainties. Similarly, the routing analysis was based on available bathymetric and topographic information rather than on detailed engineering surveys.

These simplifications do not invalidate the main comparative trends identified in this work, but they indicate that the conclusions should be understood as representative of the studied case and should be complemented in future work by full sensitivity studies, contingency analysis, and detailed project-level design refinement.

4.3. Framework Generalizability to Other Emerging Coastal Regions

Although the quantitative results reported in this study are specific to the Colombian case, the methodological framework developed here is potentially transferable to other coastal regions facing similar offshore wind integration challenges. In particular, the proposed approach may be relevant for emerging or developing power systems where offshore resources are located at medium distances from shore, grid reinforcement is limited, and transmission planning must balance technical feasibility with constrained capital investment. Comparable conditions are observed in emerging offshore wind markets such as India, where transmission planning approaches explicitly consider the trade-offs between HVAC and HVDC technologies based on distance, capacity, and system integration constraints [45].

The generalizable contribution of this work is not the adoption of a fixed 20 Hz operating frequency or a universal LFAC configuration, but rather the integrated evaluation procedure used to compare HVAC, LFAC, and HVDC alternatives under a common planning basis. This procedure combines route-specific transmission design, electrical parameter derivation, dynamic performance assessment, and comparative techno-economic analysis. As such, it can be adapted to other coastal settings by replacing the local inputs, such as seabed conditions, transmission distance, voltage standards, energy prices, and grid-code constraints, while preserving the same decision-making structure.

This type of framework may be especially valuable in regions such as Southeast Asia, West Africa, or parts of Latin America, where medium-distance offshore wind development may emerge before large-scale HVDC infrastructure becomes economically justified. In such contexts, LFAC can occupy an intermediate niche between conventional HVAC and HVDC solutions. Moreover, recent studies in emerging power systems show that high shares of renewable energy can be achieved through coordinated transmission expansion and integrated planning methodologies, even under constrained infrastructure conditions, and that such approaches are inherently replicable across different national contexts [46].

In parallel, offshore wind deployment is expanding into regions such as Southeast Asia and Latin America, supported by growing policy frameworks and infrastructure development efforts. For instance, the Philippines has established an offshore wind roadmap and approved multiple large-scale projects, while countries such as Vietnam are developing regulatory frameworks and long-term capacity targets to enable offshore wind integration. These developments illustrate that several emerging coastal systems are already progressing toward the technical and institutional conditions required to implement structured transmission planning approaches [47].

Nevertheless, the transferability of the framework should be understood at the methodological level rather than at the level of exact numerical outcomes. Parameters such as the optimal operating frequency, the number of parallel circuits, converter topology, and the relative economic ranking of the alternatives remain highly case-dependent. Therefore, while the present study supports the broader applicability of LFAC-oriented planning in emerging coastal systems, each implementation still requires site-specific electrical, regulatory, and economic reassessment.

4.4. Future Research Perspectives

Future work should evaluate LFAC system performance under non-ideal operating conditions, including fault transients, converter malfunctions, and severe voltage disturbances, as these aspects have been highlighted as critical for offshore transmission reliability [12].

Exploring advanced reactive power compensation and adaptive control strategies could further enhance voltage stability and dynamic performance [11].

Finally, optimal low-frequency selection tailored to specific route lengths and submarine–overhead mixes, may yield additional efficiency gains as suggested by [32] and [13].

5. Conclusion

This study assessed the technical and economic feasibility of a 20 Hz low-frequency alternating current (LFAC) transmission system for integrating a 960 MW offshore wind farm into Colombia's power grid. The proposed hybrid submarine–overhead link, supported by a back-to-back modular multilevel converter, met all national regulatory limits on voltage regulation and imbalance, delivered efficiencies of 94%, and provided substantially higher power transfer capability and lower shunt currents than 60 Hz HVAC. The techno-economic comparison shows that the LFAC system constitutes a technically balanced and economically viable alternative, remaining cost-competitive with HVDC while offering operational advantages for medium-distance transmission applications. These results position LFAC as a promising alternative for future offshore wind integration projects in Colombia, especially where HVAC faces reactive limitations and HVDC incurs excessive costs.

Acknowledgement

The authors acknowledge the support and infrastructure provided by the Universidad del Norte and the Universidad Distrital Francisco José de Caldas, which contributed to the completion of this research.

Funding: This research received no external funding.

Author contributions: Cristian Bernal, Valentina Fragozo, and Iván Ortega executed the numerical calculations, generated the simulation results, prepared the figures, and drafted the initial version of the manuscript (*Software, Data curation, Investigation, Visualization, Writing – original draft*) under the joint supervision of Rafael Castillo-Sierra, Mauricio Restrepo, and Juan Diego Pulgarín Rivera (*Supervision, Conceptualization, Methodology, Project administration*). All authors contributed to the analysis and interpretation of the results (*Formal analysis, Validation*). Juan Diego Pulgarín Rivera led the detailed editing and structuring of the final manuscript (*Writing – review & editing*), with additional review support from Rafael Castillo-Sierra and Mauricio Restrepo. Institutional support in infrastructure and resources was provided by Universidad del Norte and Universidad Distrital Francisco José de Caldas (*Resources*).

Disclosure statement: The authors declare no conflict of interest.

Appendix A Derivation of Generalized Reactance Expression

This section derives the expression used to extend the classical lossless power–angle relation to a mixed transmission path composed of a submarine segment and an overhead segment. The total series reactance is obtained by preserving the proportional contribution of each segment according to its length, which enables a more accurate assessment of power transfer capability under variable line configurations.

Appendix A.1 Variables

Table A1. Variables used in the generalized power–transfer derivation for a mixed submarine/overhead series path.

Symbol	Description	Unit
l	Total line length	km
f	System frequency	Hz
ω	Angular frequency, $2\pi f$	rad/s
f_{sub}	Submarine line fraction	–
f_{oh}	Overhead line fraction $(1 - f_{\text{sub}})$	–
L_{sub}	Inductance per unit length (submarine)	H/km
L_{oh}	Inductance per unit length (overhead)	H/km
x_{sub}	Reactance per unit length (submarine), ωL_{sub}	Ω/km
x_{oh}	Reactance per unit length (overhead), ωL_{oh}	Ω/km
X	Total series reactance	Ω
V_s, V_r	Sending/receiving per-phase voltage magnitudes	kV
V	Per-phase voltage used when $V_s = V_r$	kV
δ	Power angle	rad
P_ϕ	Per-phase power transfer	MW
P	Three-phase power $(3P_\phi)$	MW

Appendix A.2 Classical lossless relation

For a single series reactance X, the per-phase power is

$$P_\phi = \frac{V_s V_r}{X} \sin\delta, \tag{A1}$$

and the three-phase power is $P = 3P_\phi$. In what follows, we use the per-phase form with $V_s = V_r \triangleq V$.

Appendix A.3 Mixed-path total reactance

Let $l_{\text{sub}} = f_{\text{sub}}\, l$ and $l_{\text{oh}} = f_{\text{oh}}\, l = (1 - f_{\text{sub}})l$. The total series reactance is the length-weighted sum:

$$\begin{aligned} X &= x_{\text{sub}}\, l_{\text{sub}} + x_{\text{oh}}\, l_{\text{oh}} \\ &= \omega L_{\text{sub}}\, (f_{\text{sub}} l) + \omega L_{\text{oh}}\, \big[(1 - f_{\text{sub}})l\big] \\ &= \omega l \big[L_{\text{sub}} f_{\text{sub}} + L_{\text{oh}}(1 - f_{\text{sub}})\big] \\ &= \omega l \big[f_{\text{sub}}(L_{\text{sub}} - L_{\text{oh}}) + L_{\text{oh}}\big]. \end{aligned} \tag{A2}$$

Appendix A.4 Generalized power–angle expression

Substituting (A2) into the classical form (with $V_s = V_r = V$) yields the per-phase expression:

$$\boxed{P_\phi = \frac{V^2}{\omega\, l\, [\, f_{\text{sub}}(L_{\text{sub}} - L_{\text{oh}}) + L_{\text{oh}}\,]} \sin\delta = \frac{V^2}{2\pi f\, l\, [\, f_{\text{sub}}(L_{\text{sub}} - L_{\text{oh}}) + L_{\text{oh}}\,]} \sin\delta} \tag{A3}$$

and the corresponding three-phase power is $P = 3P_\phi$.

Appendix A.5 Notes and sanity checks

- If $f_{\text{sub}} = 0 \Rightarrow X = \omega l L_{\text{oh}}$ (pure overhead).
- If $f_{\text{sub}} = 1 \Rightarrow X = \omega l L_{\text{sub}}$ (pure submarine).
- Units: $L\,[\text{H/km}]$, $l\,[\text{km}] \Rightarrow L\,l\,[\text{H}]$; with $\omega\,[\text{rad/s}] \Rightarrow X\,[\Omega]$.

References

[1] Congreso de Colombia. Ley 1715 de 2014, 2014.

[2] The Renewables Consulting Group and ERM. Hoja de ruta para el despliegue de la energía eólica costa afuera en colombia. Technical report, Ministerio de Minas y Energía, Colombia, 2022. Prepared in collaboration with the World Bank.

[3] X. Xiang, M. M. C. Merlin, and T. C. Green. Cost analysis and comparison of hvac, lfac and hvdc for offshore wind power connection. In *12th IET International Conference on AC and DC Power Transmission (ACDC 2016)*, pages 1–6, 2016.

[4] Yongqing Meng, Shuhao Yan, Kang Wu, Lianhui Ning, Xuan Li, Xiuli Wang, and Xifan Wang. Comparative economic analysis of low frequency ac transmission system for the integration of large offshore wind farms. *Renewable Energy*, 179:1955–1968, 2021.

[5] Jonathan Ruddy, Ronan Meere, and Terence O'Donnell. Low frequency ac transmission for offshore wind power: A review. *Renewable and Sustainable Energy Reviews*, 56:75–86, 2016.

[6] P. B. Wyllie, Y. Tang, L. Ran, T. Yang, and J. Yu. Low frequency ac transmission - elements of a design for wind farm connection. In *11th IET International Conference on AC and DC Power Transmission*, pages 1–5, 2015.

[7] Sakis A. P. Meliopoulos, Dionysios Aliprantis, Yongnam Cho, Dongbo Zhao, Anupama Keeli, and Hao Chen. Low frequency transmission: Final project report. Technical Report 12-28, Power Systems Engineering Research Center (PSERC), Georgia Institute of Technology and Iowa State University, October 2012. PSERC Publication 12-28.

[8] Xin Xiang, Shiyuan Fan, Yunjie Gu, Wenlong Ming, Jianzhong Wu, Wuhua Li, Xiangning He, and Timothy C. Green. Comparison of cost-effective distances for lfac with hvac and hvdc in their connections for offshore and remote onshore wind energy. *CSEE Journal of Power and Energy Systems*, 7(5):954–975, 2021.

[9] Byeonghyeon An, Jeongsik Oh, and Taesik Park. Economic analysis of critical distance based on frequency in low frequency ac for offshore wind farms. *IEEE Access*, pages 1–1, 2025.

[10] C Nguyen Mau, K Rudion, A Orths, PB Eriksen, H Abildgaard, and ZA Styczynski. Grid connection of offshore wind farm based dfig with low frequency ac transmission system. In *2012 IEEE power and energy society general meeting*, pages 1–7. IEEE, 2012.

[11] Nan Qin, Shi You, Zhao Xu, and Vladislav Akhmatov. Offshore Wind Farm Connection with Low Frequency AC Transmission Technology. In *2009 IEEE Power & Energy Society General Meeting*, pages 1–8. IEEE, 2009.

[12] I Erlich, F Shewarega, H Wrede, and W Fischer. Low frequency AC for offshore wind power transmission – prospects and challenges. In -, pages 1–7. IET, 2015.

[13] Xin Xiang, Shiyuan Fan, Yunjie Gu, Wenlong Ming, Jianzhong Wu, Wuhua Li, Xiangning He, and Timothy Green. Comparison of cost-effective distances for LFAC with HVAC and HVDC in their connections for offshore and remote onshore wind energy. *CSEE JOURNAL OF POWER AND ENERGY SYSTEMS*, 7(5):1–22, 2021.

[14] Ming Hu, Shuhong Xie, Jianmin Zhang, and Zhijin Ma. Desing selection of dc and ac submarine power cable for offshore wind mill. In *2014 China International Conference on Electricity Distribution (CICED)*, pages 1675–1679, 2014.

[15] CIGRÉ. Power cable rating examples for calculation tool verification. Technical Brochure 880, CIGRÉ, 2022. Case Study 8, 220kV 3-core submarine export cable.

[16] International Electrotechnical Commission. IEC 60287-1-1: Electric cables - Calculation of the current rating - Part 1-1: Current rating equations and calculation of losses, 2006. Norma para evaluación térmica de cables XLPE.

[17] AIEE Committee. Soil thermal characteristics in relation to underground power cables aiee committee report. *Transactions of the American Institute of Electrical Engineers. Part III: Power Apparatus and Systems*, 79(3):792–844, 1960.

[18] Copernicus marine service - ocean data portal. https://data.marine.copernicus.eu, 2025. Accessed: 2025-05-16.

[19] Lionel Carter, Douglas Burnett, and Tara Davenport. The relationship between submarine cables and the marine environment. In Douglas R. Burnett, Lionel Carter, and Tara Davenport, editors, *Submarine Cables: The Handbook of Law and Policy*, chapter 7, pages XXX–XXX. Brill Nijhoff, Leiden, The Netherlands, 2020.

[20] International Cable Protection Committee. ICPC Recommendation No. 10: Industry Standards for Consultation, Coordination, and Spatial Separation. Technical Recommendation, n.d. Recommends parallel submarine cables maintain a separation distance of the lesser of 3 times the depth of water, or 2 times with agreement.

[21] T. Kvarts, A. C. Garolera, Z. Huang, and O. Thyrvin. Sequence impedance of submarine cables. In *CIGRÉ Session*, number 10693, Paris, France, 2022. CIGRÉ.

[22] Electric Power Research Institute. EPRI AC Transmission Line Reference Book—200 kV and Above, 2005.

[23] IEEE Power Engineering Society. IEEE Std-738-2006: Standard for Calculating the Current-Temperature Relationship of Bare Overhead Conductors, 2007. IEEE Standard.

[24] Ministerio de Minas y Energía de Colombia. RETIE 2024: Reglamento Técnico de Instalaciones Eléctricas, 2024. Resolución 40117 del 2 de abril de 2024.

[25] UNIVERSIDAD NACIONAL DE COLOMBIA. Metodología para Selección de Cable de Guarda en Líneas Aéreas de Alta Tensión, 2021.

[26] International Electrotechnical Commission. Iec 60071: International standard — insulation co-ordination, 2019.

[27] International Electrotechnical Commission. Iec 60038: International standard — iec standard voltages, 2009.

[28] International Electrotechnical Commission. Iec 60099: International standard — surge arresters, 1991.

[29] International Electrotechnical Commission. Iec 60815: International standard — selection and dimensioning of high-voltage insulators intended for service in polluted conditions, 2013.

[30] R. Marquardt and A. Lesnicar. A new modular voltage source inverter topology. *Conf. Rec. EPE 2003*, 2003.

[31] Rafael Castillo-Sierra and Jinia Roy. Active power decoupling to minimize submodule capacitance and circulating currents in modular multilevel converters. In *2024 IEEE Energy Conversion Congress and Exposition (ECCE)*, pages 57–64, 2024.

[32] David Sehloff and Line A. Roald. Low frequency ac transmission upgrades with optimal frequency selection. *IEEE Transactions on Power Systems*, 37(2):1437–1448, 2022.

[33] David Sehloff and Line Roald. Steady state modeling for variable frequency ac power flow. In *2020 52nd North American Power Symposium (NAPS)*, pages 1–6, 2021.

[34] Ronan Meere, Jonathan Ruddy, Paul McNamara, and Terence O'Donnell. Variable ac transmission frequencies for offshore wind farm interconnection. *Renewable Energy*, 103:321–332, 2017.

[35] Byeonghyeon An, Junsoo Che, Taehun Kim, and Taesik Park. Selection of an optimal frequency for offshore wind farms. *Energies*, 17(10), 2024.

[36] Peng Qiu, Xiaojun Ni, Feng Xu, Chengyu Lu, Kaijun Wang, and Wulue Pan. Optimal transmission frequency of low frequency ac system for offshore wind farm integration. In *2021 International Conference on Power System Technology (POWERCON)*, pages 1556–1560, 2021.

[37] Rafael Castillo-Sierra and Giri Venkataramanan. A comparative evaluation of power converter circuits to increase the power transfer capability of high voltage transmission lines. In *2020 52nd North American Power Symposium (NAPS)*, pages 1–6, 2021.

[38] Rafael Castillo-Sierra, Giri Venkataramanan, and Dionisio Ramirez. Control design guidelines for current-mode modular multilevel matrix converters based on dynamic modeling and stability analysis. In *2025 IEEE Workshop on Power Electronics and Power Quality Applications (PEPQA)*, pages 1–8, 2025.

[39] Rafael Castillo-Sierra, Giri Venkataramanan, and Dionisio Ramirez. Small-signal stability analysis of droop-controlled point-to-point low-frequency ac transmission lines. In *2023 IEEE Energy Conversion Congress and Exposition (ECCE)*, pages 2301–2308, Nashville, TN, USA, 2023. IEEE.

[40] CREG. Resolución creg 025 de 1995: Por la cual se establece el reglamento de calidad del servicio de energía eléctrica, 1995.

[41] ICONTEC. NTC 5001: Código Eléctrico Colombiano, 2011. Norma Técnica Colombiana.

[42] ABB Semiconductors Ltd. *Reverse Conducting Integrated Gate-Commutated Thyristor (RC-IGCT) 5SHX 36L4521 – Preliminary Data Sheet*. ABB Switzerland Ltd, Semiconductors, Lenzburg, Switzerland, 2020. Preliminary data sheet.

[43] Jovana Dakica, Marc Cheah-Manea, Oriol Gomis-Bellmunt, and Eduardo Prieto-Araujo. Low frequency ac transmission systems for offshore wind power plants: Design, optimization and comparison to hvac and hvdc. *CITCEA-UPC, Department of Electrical Engineering, Universitat Politècnica de Catalunya*, 2021. Technical report.

[44] Jian Liu, Dong Dong, and Di Zhang. A hybrid modular multilevel converter family with higher power density and efficiency. *IEEE Transactions on Power Electronics*, 36(8):9001–9014, 2021.

[45] Government of India, Ministry of Power, and MNRE. India roadmap for offshore wind power evacuation and grid integration. Technical report, Accelerating Smart Power and Renewable Energy (ASPIRE) Programme, 2023. Offshore wind transmission planning and evacuation framework study.

[46] Nicolo Stevanato, Valeria Baiocco, and Emanuela Colombo. Calliope africa: Modeling the role of storage and transmission for renewable energy integration. *Energy for Sustainable Development*, 88, 06 2025.

[47] Global Wind Energy Council, Rebecca Williams, Feng Zhao, Nina Melkonyan, Mark Hutchinson, and Janice Cheong. Global offshore wind report 2025, June 2025.